

The Lanthanide Tetrad Effect in Argillic Alteration: An Example from the Jizvan District, Northern Iran

Ali ABEDINI^{1,*}, Mansour REZAEI AZIZI¹ and Ali Asghar CALAGARI²

¹ Department of Geology, Faculty of Sciences, Urmia University, 5756151818, Urmia, Iran

² Department of Earth Sciences, Faculty of Natural Sciences, University of Tabriz, 5166616471, Tabriz, Iran

Abstract: Intrusion of quartz-monzodioritic igneous bodies of Oligocene age into Eocene lithic crystal tuffs and trachy-basalts resulted in the occurrence of a widespread argillic alteration zone in the Jizvan district (northern Iran). Mineralogically, the argillic alteration zone includes minerals such as kaolinite, quartz, smectite, pyrophyllite, muscovite-illite, alunite, rutile, calcite, feldspar, chlorite, hematite and goethite. Therefore, the non-CHARAC behaviour for trace elements in the argillic samples is reflected in the non-chondritic Y/Ho and Zr/Hf ratios and the irregular REE patterns, which appear related to the tetrad effect phenomenon. The chondrite-normalized REE distribution patterns indicate both concave (W-shaped) and convex (M-shaped) tetrad effects in the argillic samples. Based on the field evidence and the results from geochemical studies, it can be concluded that the samples from the argillic alteration zone having high fourth tetrad effect values (>0.30) were developed in the fault and breccia zones. The results indicate that factors such as preferential scavenging by Mn-oxides, crystallization of clay minerals, fluid-rock interaction, overprint of hypogene mineral assemblage by supergene ones, and the structural control, have all played an important role in the occurrence of tetrad effects in samples of the argillic zone in the Jizvan district.

Key words: REE geochemistry, tetrad effect, argillic alteration, Jizvan, Iran

1 Introduction

Lanthanides known as rare earth elements (REE) are a group of elements from La to Lu which display similar geochemical behaviors in various geological environments. They exist in a trivalent oxidation state, except for cerium and europium (Censi et al., 2007). On the other hand, lanthanide contraction means that their atomic radius decreases from 1.03 Å (La, with atomic number of 57) to 0.86 Å (Lu, with atomic number of 71) for 6-fold coordination (Shannon, 1976). This feature of the lanthanides causes their ionization potential to be gradually increased from light REE (LREE: from La to Eu) toward heavy REE (HREE: from Gd to Lu). Geochemically isovalent trace elements such as Y-Ho and Zr-Hf distribution in geochemical systems can be controlled by their ionic radius and charge, defined as CHARAC (charge-radius control) behavior. As a result, smooth distribution patterns are produced due to their CHARAC behavior during geochemical processes (Bau,

1996). During geochemical processes, irregular patterns of normalized REE are also observed, which are related to non-CHARAC (non charge-radius control) behavior (Monecke et al., 2002). Recently, this feature was labeled as “tetrad effect”, “double-double feature”, or “Zigzag or kinked pattern” (Fidelis and Siekierski, 1966; Peppard et al., 1969), which were used by various researchers (Lee et al., 1994; Takahashi et al., 2002; Zhao et al., 2002; Liu and Zhang, 2005; Takahashi et al., 2005; Feng, 2010; Lee et al., 2010; Peretyazhko and Savina, 2010; Pérez-López et al., 2010; Abedini et al., 2017; Rezaei Azizi et al., 2017). Based on geochemical investigations in various geological environments, two conspicuous forms of REE distribution patterns - so-called convex (M-shaped) and concave (W-shaped) tetrad effects - have been reported. The convex (M-shaped) tetrad effect forms are mostly reported from igneous and related systems such as hydrothermal alterations, and the concave (W-shaped) forms in normalized REE distribution patterns are generally observed in low temperature deposits such as phosphorites, limestones, marine sediments and cherts (Masuda et al., 1987; Lee et al., 1994; Akagi et al., 2004;

* Corresponding author. E-mail: abedini2020@yahoo.com

Peretyazhko and Savina, 2010; Feng et al., 2014; Censi et al., 2016). The tetrads are named as the first (from La to Nd), the second (from Pm to Gd), the third (from Gd to Ho) and the fourth (from Ho to Lu). Gd is the only lanthanide which is common to the second and third tetrads. It has been proved that the cusps in the normalized curve of REE distribution pattern are due to quarter, half, three quarter, and complete filling of the $4f$ orbital of lanthanides (Jahn et al., 2001). Many researchers have proposed theories to interpret this feature in geochemical systems, with the main mechanisms proposed as follows (Jørgensen, 1970; Masuda et al., 1994; Kawabe et al., 1999; Censi et al., 2007): (1) electron structure in REE, (2) nephelauxetic effect, (3) the quantum base theory of Gibbs, and (4) a theory based on spin energy.

Alteration zones are commonly associated with mineral deposits, such as precious and base metals formed during hydrothermal processes (Ekosse, 2001; Domínguez et al., 2010; Zhang and Smith-Duque, 2014; Dill et al., 2015; Veliz et al., 2017; Watanabe et al., 2018). Generally, the formation of intermediate argillic zones is attributed to hypogene near-surface epithermal, geothermal activities (hot springs), and supergene environments (Abedini and Calagari, 2015; 2016). Therefore, the argillic alteration development in an area can be used as an exploration tool for sub-surface deposits particularly for Cu-Au high-sulfidation and porphyry-type deposits (Lerouge et al., 2006; Lin et al., 2017).

The Cenozoic magmatic activities and associated alterations and ore mineralization in the Alborz-Azarbaidjan belt (N-NW Iran) have been shown to be related to the subduction and assimilation of the Arabian plate beneath the Eurasian plate during the major Alpine orogenic phases (Calagari, 2004; Mehrabi et al., 2016). According to these authors, there are two metallogenic provinces along this belt: (1) Ahar-Arasbaran (in the north of the belt) and (2) Tarom-Hashtjin (to the south of the belt). The Tarom-Hashtjin metallogenic province (western Alborz) in northern Iran accommodates many base metal deposits, and hence is a suitable locality to prospect for these metals. This province comprises several intrusive rocks which are classified as I-type granites of Cordilleran age (Jafarzadeh et al., 2014). Some copper mineralizations in the Taleghan area within plutonic (monzonite) and volcanic rocks along with various epithermal deposits in Mesbolaghi, Rashtabad, Agjeeh Gale and Glojeh areas have been reported from this metallogenic province by Darabi-Golestan and Hezarkhani (2016). These workers suggested that the granitoids of these areas are responsible for various Fe and Cu mineralizations. Intrusion of Oligocene igneous bodies into Eocene igneous complexes produced widespread argillic alteration zones and

accompanying base and precious metal mineralizations in this province.

The Jizvan district is a part of the Tarom-Hashtjin metallogenic province. The occurrence of extensive hydrothermal alteration zones in this province was likely due to the intrusion of Oligocene quartz-monzonitic bodies into the Eocene lithic crystal tuffs and trachy-basalts. Development of widespread argillic alteration zones in the Jizvan district is also a result of this intrusion. The argillic zones include silicic veins and veinlets in which Fe and Cu mineralizations are observed. The main aim of this paper is to consider the REE geochemistry in the lithic crystal tuffs and the argillic alteration zones in the study area, in order to evaluate the use of the tetrad effect as a new tool in geochemical investigations and interpretations.

2 Geological Setting

The deep subduction of a slab of Arabian plate in northwestern Iran during the Late Cretaceous-Early Paleogene is considered to be the main reason for the development of an extensional zone in the Alborz-Azarbaidjan belt. A back-arc subducting micro-slab beneath the Alborz-Azarbaidjan belt in the Khoy district during the Late Cretaceous-Early Paleogene (Khalatbari-Jafari et al., 2003) generated the magmatic arc in this part of the belt during the early Eocene (Darabi-Golestan and Hezarkhani, 2016). Consequently, due to the emplacement of various igneous bodies in this district during the Oligocene, a wide range of altered lithologies, including the argillic alteration zones of Jizvan district, were developed.

As illustrated in Fig. 1, the Jizvan district is considered as a part of the Alborz-Azarbaidjan structural zone (Nabavi, 1976), which comprises various rock types that range in age from the Eocene to the Quaternary. The E-W trending of the Alborz-Azarbaidjan structural zone, known as the magmatic belt, includes the N-S trending Rasht-Takestan fault, which separates the eastern part from the western part (Azizi and Moinevaziri, 2009). The west side of this fault is characterized by the presence of andesitic to dacitic lava flows and some high-K to shoshonitic granitoids, whereas the east side comprises mostly mafic to felsic tuffs and lavas (Nabatian et al., 2014; Darabi-Golestan and Hezarkhani, 2016). The west side of this fault (Alborz-Azarbaidjan structural zone) includes two separate metallogenic provinces: (1) the Ahar-Arasbaran (in the north) and (2) the Tarom-Hashtjin (in the south).

The simplified geological map of the Jizvan district and the sampling line are illustrated in Fig. 2a–b. The studied Jizvan district is located in the Tarom-Hashtjin metallogenic province, western Alborz (Jafarzadeh et al.,

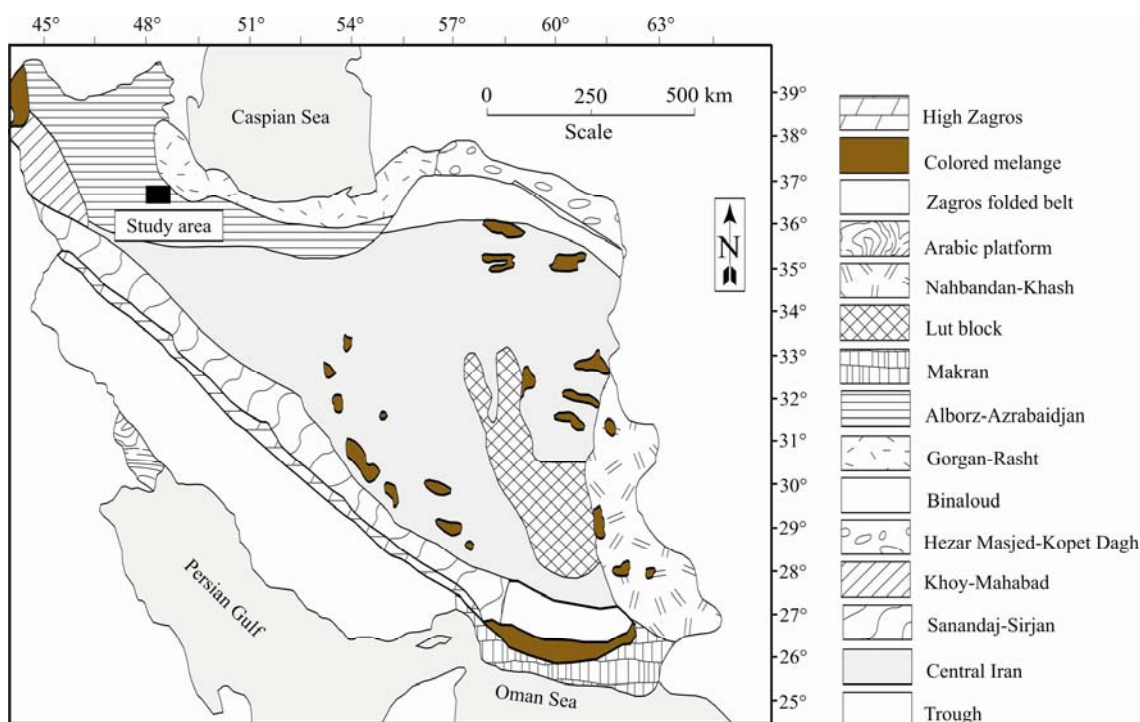


Fig. 1. Simplified geological map showing the 15 structural zones of Iran (after Nabavi, 1976) and the location of the study area (the Jizvan district).

2014). Previous geological work revealed that numerous I-type intrusive rocks (granite, granitoid, quartz-monzonite) and volcanic to sub-volcanic rocks (rhyodacite, rhyolite, andesitic basalt, andesite, trachyandesite, trachydacite, basalt, tuff, rhyolitic tuff) are present in most parts of the Taram-Hashtjin metallogenic province (Darabi-Golestan and Hezarkhani, 2016). They are associated with numerous Fe and Cu mineralizations. According to Mehrabi et al. (2014), most of the igneous rock types in this district have a typically high-K calc-alkaline to shoshonitic character.

As shown in Fig. 2a, the Jizvan district is mostly covered by igneous rocks of various compositions from Eocene to Oligocene ages. The lithological units of the studied district, from the oldest to the youngest, are lithic crystal tuffs and trachy-basalt (Eocene) covering most of the district, andesitic to trachy-andesitic lava (Eocene), quartz-monzodiorite (Oligocene), andesi-basalt (Oligocene), trachyte (Plio-Quaternary), and finally recent alluvia (Quaternary). Field observations revealed that the lithic crystal tuffs and trachy-basalts of the studied district became extensively altered, displaying mainly vein/veinlet-type of Cu-Fe-Pb mineralization. Field relationships clearly show that alteration zones are intimately and predominantly associated with brecciated fault zones, which acted as permeable channels for ascending hydrothermal fluids. Three types of alteration zone were recognized in this district (see Fig. 2a): (a) argillic, (b) phyllic, and (c) propylitic. Among these, argillic alteration

zones are dominant and widespread in the studied district.

3 Sampling and Methodology

For mineralogical and geochemical studies, a transect (~550 m) across the lithic crystal tuffs and the argillic alteration zone was selected for sampling purposes. To investigate the geochemical behavior of lithic crystal tuff, two representative samples (P-1 and P-2) were collected (Fig. 2b). 14 samples (N-1 to N-14) were taken as representative samples of argillic alteration for geochemical studies (Fig. 2b). Among argillic samples, N-7, N-8, and N-9 were on the fault zone and N-12, N-13, and N-14 samples were on the breccia zone (Fig. 2b).

Petrographic examinations were carried out on 14 thin-polished sections of the lithic crystal tuffs using a polarizing microscope. Meanwhile, for identification of unknown mineral phases in the argillic alteration zone, 5 samples were chosen for X-ray diffraction (XRD) analyses performed at the Geological Survey of Iran by using a D-5000 SIEMENS diffractometer using $\text{CuK}\alpha$ radiation and a 1° 2θ per minute scanning rate, 40 kV, and 40 mA. For determination of whole-rock chemical composition, all samples were dried at 60°C and then crushed and pulverized to a particle size of less than 150 mesh (<100 microns) in a steel mill.

Two samples from the lithic crystal tuffs and 14 samples from the argillic alteration zone were collected at about 25 m intervals along the transect (Fig. 2b) for

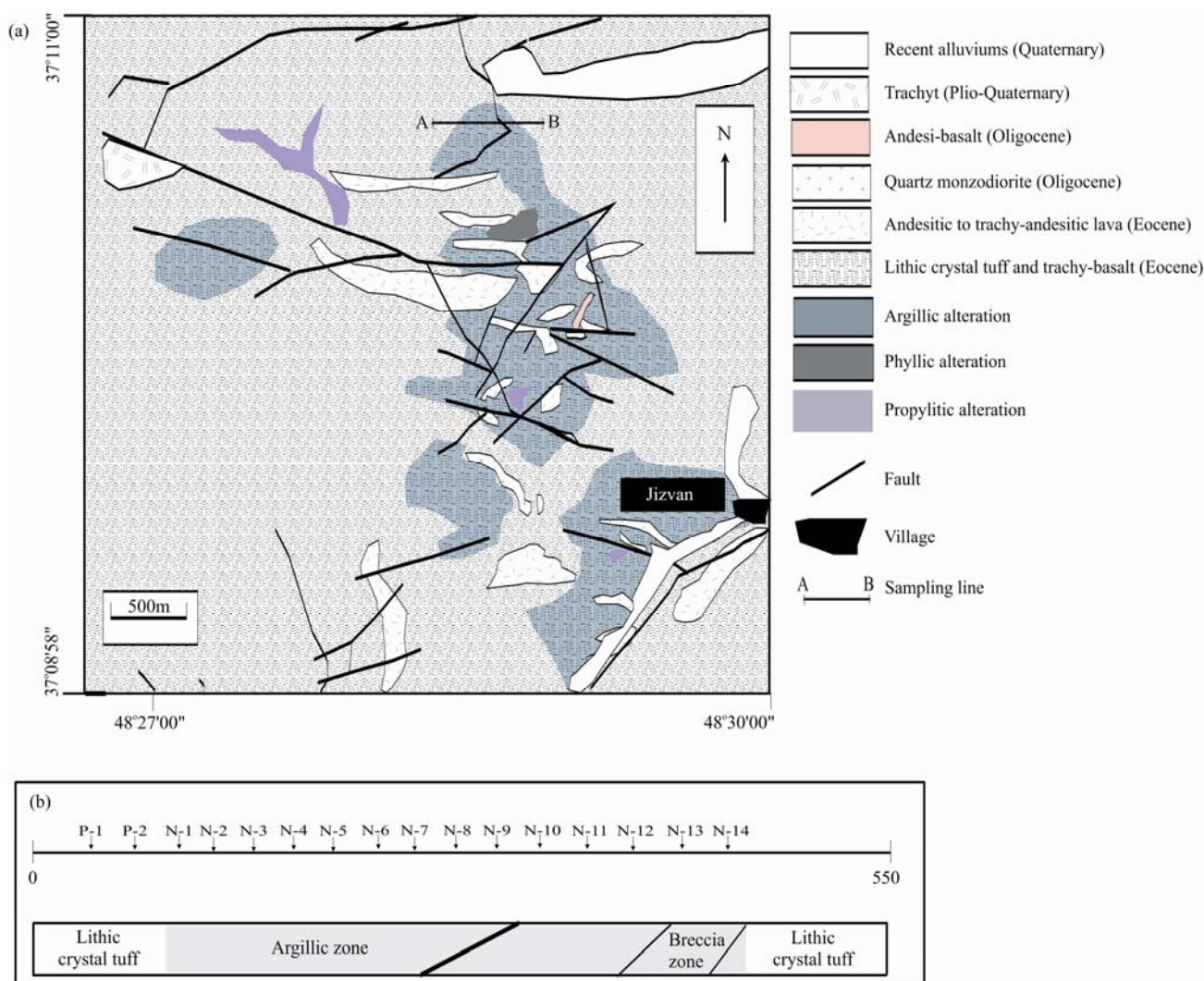


Fig. 2. Geological and sampling profile of the Jizvan district.

(a), Geological map of the studied district displaying the location of the argillic, phyllic, and propylitic alteration zones and the enclosing rocks. (b), the sampling line showing the position of the collected samples.

geochemical analyses. The concentrations of major oxides and trace elements were determined using the inductively coupled plasma emission spectroscopy (ICP-ES) method at the ACME Analytical Laboratories Ltd., Vancouver, Canada. Rare earth element concentrations of the collected samples were determined by inductively coupled plasma mass spectrometry (ICP-MS) method at the same laboratory (ACME). The concentration of major oxides and trace/rare earth elements are given in wt% (weight percent) and parts per million (ppm), respectively. The detection limits of major oxides, minor/trace elements, and rare earth elements varies between 0.002–0.04 wt%, 0.1–20 ppm, and 0.01–0.03 ppm, respectively. For determination of the LOI (loss on ignition), 1 gram of each sample was heated at 950°C for 90 minutes, and then the weight loss during this process was calculated as LOI. All the computations and plots in this research were carried out by using MATLAB R2012b software.

4 Results

4.1 Mineralogical and petrographical aspects

The results of X-ray diffraction (XRD) analyses show pronounced peaks for kaolinite and quartz (Fig. 3) as the main mineral phases in the argillic samples. As the XRD results illustrate, the minor mineral phases in the argillic samples are hematite, muscovite-illite, rutile, chlorite, goethite, alunite, smectite, pyrophyllite, calcite and feldspar.

Petrographic examination showed that the parent rocks for the argillic alteration zones are the lithic crystal tuffs which have a predominantly andesitic composition and show microlithic and porphyritic textures. These rocks have phenocrysts of plagioclase, clinopyroxene and hornblende dispersed in a microlithic matrix consisting of plagioclase, chlorite, calcite and epidote. Zircon and apatite are two accessory minerals present within the

matrix. Epidote, chlorite, calcite and pyrite are the important alteration products.

The silicic-carbonate veins/veinlets within the argillic alteration zone contain chalcopyrite, covellite, pyrite (Fig. 4a), hematite (Fig. 4b), galena (Fig. 4c), goethite (Fig. 4d), malachite and azurite minerals.

4.2 Major oxide variations

Table 1 lists the concentration values of major oxides in samples from the lithic crystal tuffs and the argillic alteration zone in the Jizvan district. The values of SiO_2 vary within the range of 63.64–65.32 wt% and 53.11–68.84 wt% in the lithic crystal tuffs and argillic samples, respectively. The concentrations of Al_2O_3 and Fe_2O_3 in the lithic crystal tuffs range from 14.95 to 15.83 wt% (mean of 15.39 wt%) and from 4.97 to 5.04 wt% (mean of 5.00 wt%), respectively. These oxides in samples of the argillic alteration zone are within the range of 16.52–33.67 wt% (mean of 21.93 wt%) and 0.51–0.95 wt% (mean of 0.78 wt%), respectively.

The concentrations of CaO , Na_2O , MgO and K_2O in the lithic crystal tuffs show ranges of 3.03–3.69 wt%, 4.36–4.58 wt%, 1.97–2.43 wt%, and 2.34–2.74 wt%, respectively. Meanwhile, the corresponding values in the

argillic alteration zone have ranges of 0.19–0.78 wt%, 0.34–1.87 wt%, 0.06–0.37 wt%, and 0.75–1.78 wt%, respectively. The TiO_2 concentration values in both rock types (the lithic crystal tuffs and the argillic alteration zone) are very low and vary in abundance within the range of 0.08–0.81 wt%. The MnO , Cr_2O_3 and P_2O_5 concentration values in samples from the lithic crystal tuffs and the argillic alteration zone are also low, and have ranges of 0.09–0.91 wt%, 0.033–0.93 wt%, and 0.03–0.22 wt%, respectively. Finally, the LOI values of all samples vary from 1.13 to 10.58 wt%.

Graphically, SiO_2 and Al_2O_3 values show a relatively constant trend in samples from the argillic zone, but slight variations of SiO_2 and Al_2O_3 occurred in samples N-7, N-8 and N-9, in the range of 53.11–58.03 wt% and 27.96–33.67 wt%, respectively (Fig. 5a). The N-7, N-8, and N-9 samples also showed similar variations for the concentration values of other major elements (Fig. 5b).

4.3 Trace/rare earth element variations and geochemical ratios

Table 2 lists the values of trace elements (including REE) and geochemical ratios. Among trace elements, the Y, Zr, Ta, Nb, and Hf concentrations vary within the range

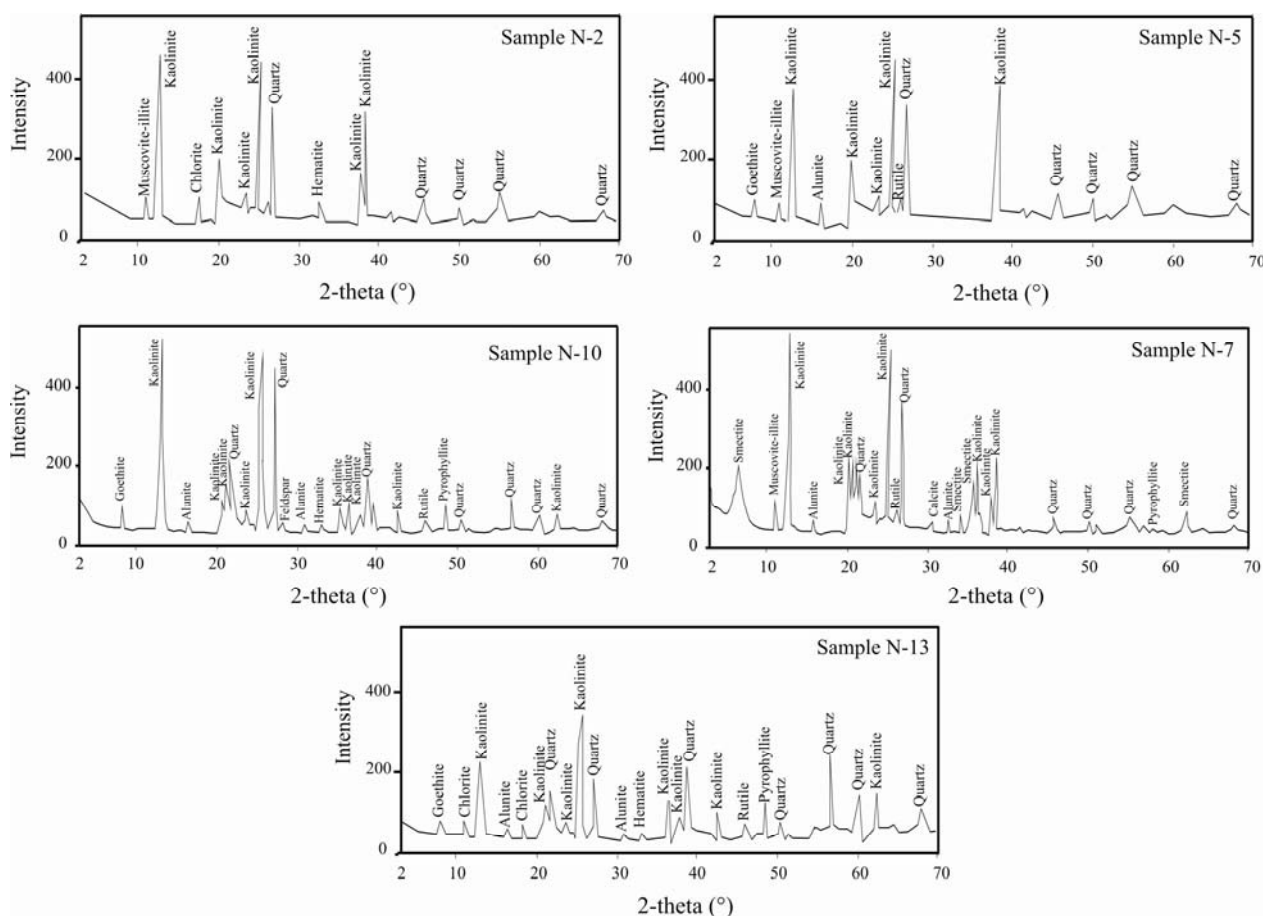


Fig. 3. X-ray diffraction (XRD) results of the samples from the argillic alteration zone in the studied district.

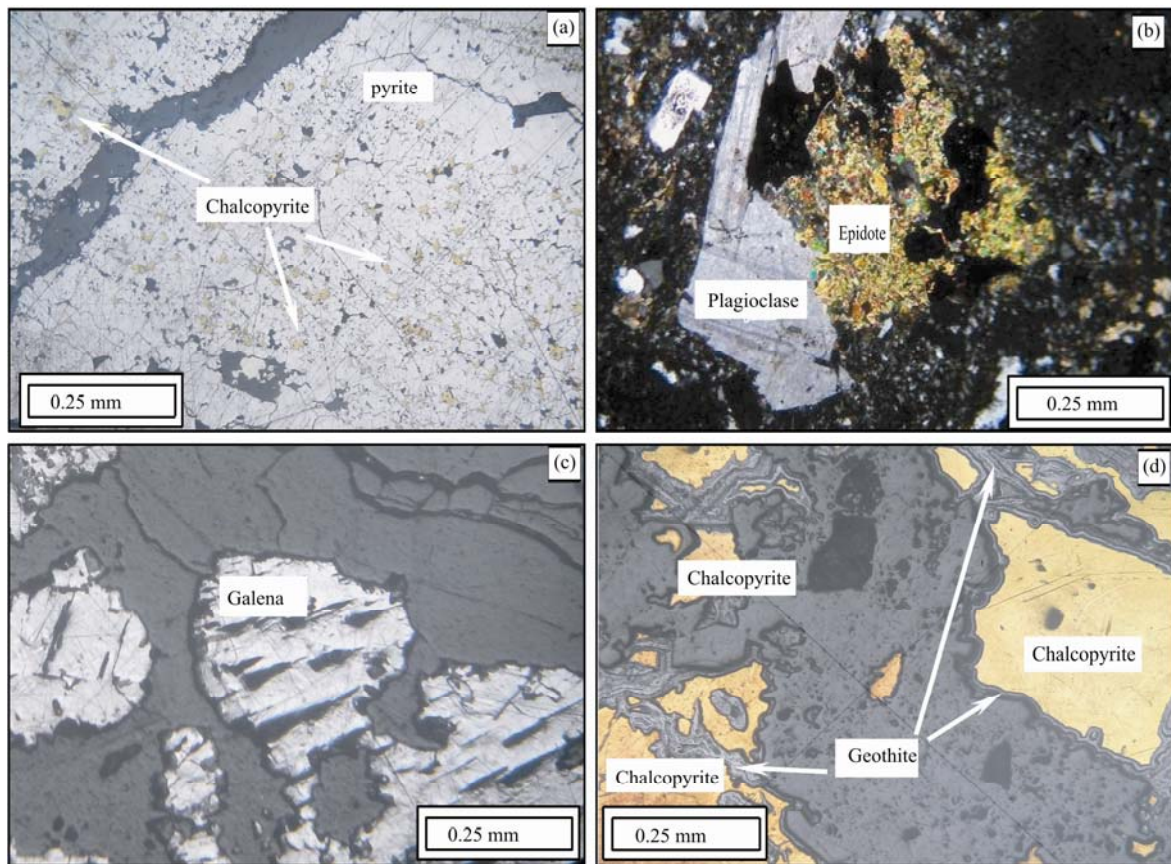


Fig. 4. Photomicrographs of the opaque (sulfide and oxide) minerals within the quartz-carbonate veinlets of the argillic alteration zone in the Jizvan district. (a), presence of anhedral chalcopyrite, covellite, and pyrite. (b), platy and tabular hematite. (c), galena co

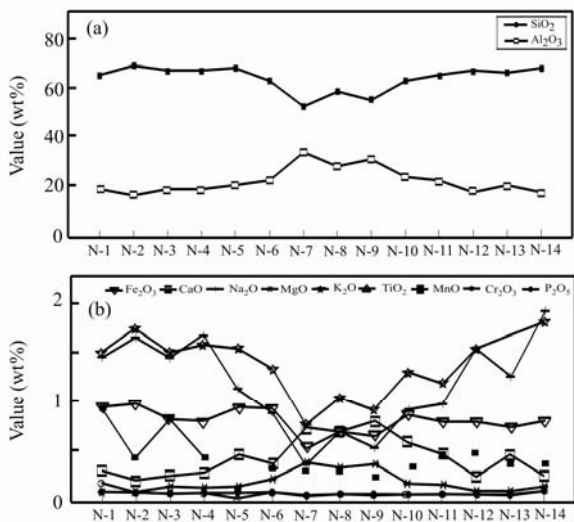


Fig. 5. Representation of the abundance of the major oxides in the argillic samples of the Jizvan district. (a), For Al₂O₃ and SiO₂. (b), For Fe₂O₃, CaO, Na₂O, MgO, K₂O, TiO₂, MnO, Cr₂O₃ and P₂O₅.

of 10.1–27.7 ppm (mean of 15.22 ppm), 24.2–165.2 ppm (mean of 64.76 ppm), 0.7–1.2 ppm (mean of 0.89 ppm), 9.2–14.4 ppm (mean of 11.79 ppm), and 2.1–4.5 ppm (mean of 3.89 ppm), respectively. Meanwhile, the SREE

concentration of the samples are relatively low and vary from 120.86 to 195.01 ppm (mean of 156.95 ppm). Σ LREE and Σ HREE are within the range of 100.25–180.98 ppm and 13.97–23.99 ppm, respectively.

As Fig. 6a shows, REE and LREE concentration values for the argillic unit show variations for samples from N-1 to N-6; almost no variation for samples N-7, N-8, and N-9; and slight variation for the rest of the samples. As shown in Fig. 6b, HREE and LREE/HREE ratios are relatively constant. As Fig. 6c shows, the La/Lu ratios of the analyzed samples (except samples N-1 and N-14) vary in the narrow range of 8.25–12.81 (average of 11.15). This means that the LREE contents of the samples decrease along the profile, whereas the HREE contents remain relatively constant. Meanwhile, the La/Lu ratios for the N-1 and N-14 samples are 37.73 and 25.23, respectively. The Zr/Hf and Nb/Ta ratios of the argillic samples vary from 6.72 to 17.82 and from 7.67 to 18.71, respectively. As Fig. 6c displays, the Zr/Hf ratios of N-7, N-8, and N-9 samples have maximum values which are within the range of 15.37–17.82, whereas this ratio for other samples of the argillic zone are within the range of 6.72–14.52. The Nb/Ta ratios of N-7, N-8, and N-9 samples in the argillic zone have lower values which are within the range of 7.67–10.78,

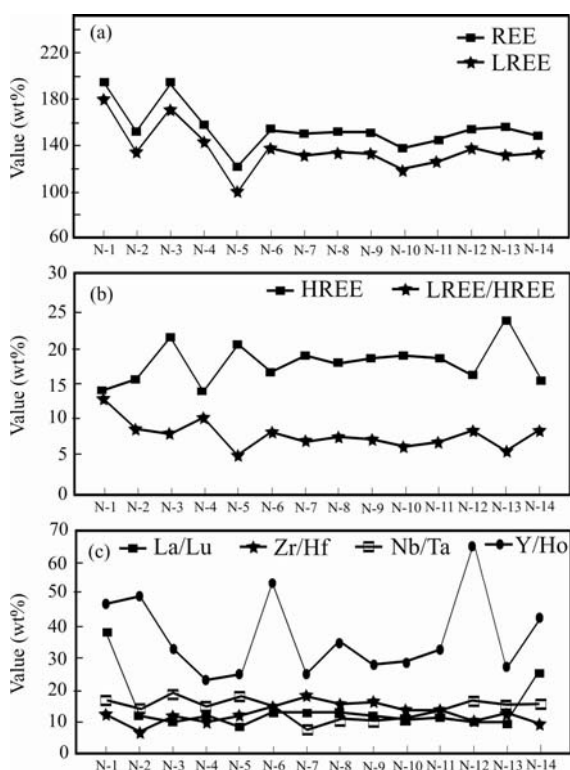


Fig. 6. The variation diagrams in Jizvan district.

(a), concentration values of REE and LREE. (b), concentration values of HREE along with ratios of LREE/HREE. (c), Representation of La/Lu, Zr/Hf, Nb/Ta and Y/Ho values as geochemical parameters in samples from the argillic zone of the studied profile.

whereas the values of Nb/Ta ratios for other samples are within the range of 11.09–18.71. Based upon the results, it is clear that the Y/Ho ratios of all samples from the argillic zone show wide variations within the range of 22.9–65.91.

4.4. The Ce and Eu anomalies

To calculate the Ce and Eu anomaly values in samples from the argillic unit and the lithic crystal tuffs, the following equations were used (Bau and Dulsky, 1995; Monecke et al., 2000):

$$\text{Eu}/\text{Eu}^* = \text{Eu}_N / \sqrt{(\text{Sm}_N \times \text{Gd}_N)} \quad (1)$$

$$\text{Ce}/\text{Ce}^* = \text{Ce}_N / \sqrt{(\text{La}_N \times \text{Pr}_N)} \quad (2)$$

In these equations, normalization values of elements (N) are from Anders and Grevesse (1989). The calculated Ce and Eu anomaly values are shown in Table 2, and vary within the range of 0.52 to 1.03 and 0.23 to 0.75, respectively in samples from the argillic zone. The equivalent values in the lithic crystal tuff samples are within the range of 0.94–1.0 and 0.99–1.01, respectively.

5 Discussion

5.1 Trace and rare earth element distribution patterns

Investigations of lithophile trace elements such as Y, Zr, Nb, Ta, as well as REE in various rocks and environments, can be useful to better understand the deposit geochemistry and Earth evolution (Rezaei Azizi et al., 2017). Hydrothermal alteration causes mobilization of most trace elements, due to the dissolution of minerals and the formation of new mineral phases (El-Mezayen et al., 2015). Among trace elements, Y (1.015 Å) and Ho (1.019 Å), both in trivalent oxidation states, have similar geochemical behavior in different geological environments (Gadd et al., 2016). Meanwhile, Zr-Hf and Nb-Ta are geochemically similar pairs with equal charge and a similar ionic radius. Despite the similar behavior of Zr and Hf, the variation of the Zr/Hf ratio in a geochemical system can be attributed to fractional crystallization, hydrothermal solutions, fluids responsible for metamorphism, and tetrad effect (Bau, 1996; Tang et al., 2014; Rezaei Azizi et al., 2017). REE distribution in the geological environments is controlled by charge and radius (so-called CHARAC behavior) of these elements (Bau, 1996). This means that irregular normalized distribution patterns can be attributed to non-CHARAC behavior of lanthanides during geochemical processes which cause them to be partitioned into four different groups (Monecke et al., 2002). Geochemical investigations have shown that superchondritic values of Y/Ho can be indicative of hydrothermal activities, complexation, and fluid-rock interaction (Bau, 1996; Uysal et al., 2011).

The behaviors of Zr, Hf, Y, and Ho are generally controlled by CHARAC behavior and the chondritic ratios for Y/Ho and Zr/Hf have ranges of 24–34 and 26–46, respectively (Bau, 1996). The Zr/Hf and Y/Ho ratios of the collected argillic samples in the studied district display non-CHARAC behavior (Fig. 7). Shown in this figure are also superchondritic Zr/Hf ratios and chondritic Y/Ho ratios in a lithic crystal tuff sample. In contrast, the Zr/Hf ratios of the argillic samples are subchondritic and the Y/Ho ratios display wide variations within the range of chondritic to superchondritic values. Particle reactivity of Ho relative to Y in various geochemical processes such as aqueous and other environments causes Ho to be scavenged preferentially by Fe- and/or Mn-oxides (hydroxides) (Bau, 1996; Bau et al., 1996; Koschinsky et al., 1997). Moreover, during weathering conditions the Y/Ho ratios increase (44–74), due to surface complexation and/or increasing the solubility of Y relative to Ho (Nozaki et al., 1997). Therefore, it can be concluded that some of the argillic samples, including N-1, N-2, N-6, N-12 and N-14, with high Y/Ho ratios (42.16–65.91) were altered under weathering conditions, and other samples display Y/Ho ratios near to chondritic values. The Zr/Hf values of the N-7, N-8 and N-9 samples are relatively higher (within the range of 15.37–17.82), whereas the

Table 1 Concentration values of the major oxides and LOI (loss on ignition) in samples from the lithic crystal tuffs (samples P-1, P-2) and the argillic alteration zone (samples N-1 to N-14) in the Jizvan district (The values are in wt%)

Sample No	Detection limit	P-1	P-2	N-1	N-2	N-3	N-4	N-5	N-6	N-7	N-8	N-9	N-10	N-11	N-12	N-13	N-14
SiO ₂	0.01	63.64	65.32	65.33	68.84	66.84	66.78	67.88	63.11	53.11	58.03	55.61	63.25	64.78	66.52	66.22	68.02
Al ₂ O ₃	0.01	15.83	14.95	18.61	16.52	18.43	18.21	19.56	22.28	33.67	27.96	30.72	23.88	21.84	18.17	20.03	17.09
Fe ₂ O ₃	0.04	5.04	4.97	0.91	0.95	0.79	0.78	0.93	0.91	0.51	0.68	0.63	0.84	0.78	0.77	0.72	0.78
CaO	0.01	3.69	3.03	0.29	0.19	0.23	0.26	0.45	0.35	0.71	0.26	0.78	0.56	0.45	0.23	0.45	0.78
Na ₂ O	0.01	4.58	4.36	1.42	1.61	1.42	1.64	1.09	0.88	0.34	0.68	0.52	0.88	0.95	1.51	1.24	1.87
MgO	0.01	2.43	1.97	0.08	0.06	0.14	0.12	0.13	0.21	0.37	0.32	0.36	0.16	0.15	0.09	0.09	0.13
K ₂ O	0.01	2.34	2.74	1.47	1.71	1.46	1.55	1.51	1.31	0.75	1.02	0.89	1.27	1.16	1.51	1.64	1.78
TiO ₂	0.01	0.81	0.69	0.08	0.09	0.12	0.33	0.22	0.33	0.41	0.36	0.37	0.28	0.32	0.22	0.23	0.09
MnO	0.01	0.19	0.17	0.91	0.41	0.82	0.43	0.09	0.31	0.29	0.28	0.23	0.32	0.45	0.46	0.36	0.36
Cr ₂ O ₃	0.002	0.093	0.087	0.068	0.071	0.066	0.071	0.073	0.066	0.033	0.061	0.052	0.059	0.061	0.051	0.054	0.064
P ₂ O ₅	0.01	0.22	0.18	0.16	0.08	0.06	0.07	0.03	0.08	0.05	0.06	0.07	0.05	0.06	0.07	0.03	0.09
L.O.I	-	1.13	1.51	10.58	9.45	9.55	9.84	7.99	10.16	9.72	9.75	9.71	8.38	8.94	10.18	8.81	9.41
Sum	-	99.993	99.977	99.908	99.981	99.926	99.881	99.953	99.996	99.963	99.871	99.942	99.929	99.941	99.781	99.874	99.914

Table 2 Concentration values of REE and some trace elements of the studied samples from the lithic crystal tuffs (samples P-1, P-2) and the argillic alteration zone (samples N-1 to N-14) in the Jizvan district. The detection limits for each element are also given (The values are in ppm)

Sample No	Detection limit	P-1	P-2	N-1	N-2	N-3	N-4	N-5	N-6	N-7	N-8	N-9	N-10	N-11	N-12	N-13	N-14
U	0.1	5.4	5.1	3.2	3.5	3.2	3.7	3.8	3.5	2.6	3.1	2.8	3.2	3.2	3.5	3.2	3.4
Y	0.1	27.7	23.1	14.5	14.2	14.4	14.2	13.3	16.5	10.1	13.2	11.6	13.1	13.5	14.5	14.1	15.6
Zr	0.1	165.2	159.2	46.2	24.2	48.2	40.1	47.8	55.2	78.4	66.1	72.1	56.4	51.4	41.3	49.2	35.1
Ta	0.1	1.1	1.1	0.7	0.9	0.7	0.9	0.8	0.9	1.2	0.9	0.9	1.1	0.8	0.7	0.7	0.8
Nb	0.1	12.5	12.2	11.5	12.8	13.1	13.2	14.4	13.1	9.2	9.7	9.4	12.2	10.8	11.5	10.6	12.5
Hf	0.1	2.1	3.7	3.8	3.6	4.2	3.9	4.1	3.8	4.4	4.3	4.5	4.2	3.9	4.1	3.9	3.7
La	0.1	39.8	34.5	40.1	21.2	32.3	27.5	23.1	23.5	23.5	23.4	24.1	25.4	24.5	24.1	26.5	26.8
Ce	0.1	72.2	67.5	64.1	37.2	53.2	45.1	42.1	42.9	39.9	40.6	39.8	41.2	40.9	44.2	45.2	46.5
Pr	0.02	8.45	7.52	8.91	14.02	4.77	9.42	5.88	4.77	6.03	5.41	5.69	5.64	5.51	7.81	7.41	11.05
Nd	0.3	33.7	28.6	49.4	51.8	58.7	43.1	20.6	52.6	51.9	52.3	52.4	36.5	44.4	48.5	46.2	33.51
Sm	0.05	6.04	5.17	15.91	9.02	21.52	18.32	6.81	11.73	9.34	10.52	9.91	8.66	9.54	12.54	5.41	14.04
Eu	0.02	1.87	1.54	2.56	1.91	1.41	1.03	1.76	2.45	1.05	1.76	1.43	1.76	1.78	0.91	1.51	1.41
Gd	0.05	5.21	4.32	6.82	7.76	15.71	5.67	12.93	10.53	8.95	9.72	9.32	11.32	10.52	9.02	13.41	6.52
Tb	0.01	0.83	0.67	1.24	0.91	1.25	1.03	1.21	1.02	1.84	1.43	1.65	1.31	1.37	1.07	2.77	1.71
Dy	0.05	5.06	4.21	2.79	3.04	1.05	1.81	2.02	2.38	3.88	3.13	3.51	2.57	2.85	2.82	3.95	3.12
Ho	0.02	0.99	0.81	0.31	0.29	0.44	0.62	0.54	0.31	0.41	0.38	0.41	0.46	0.42	0.22	0.53	0.37
Er	0.03	2.86	2.36	1.43	1.95	1.08	2.32	1.58	1.07	2.32	1.69	2.01	1.62	1.65	1.88	0.99	2.02
Tm	0.01	0.42	0.35	0.18	0.23	0.21	0.27	0.27	0.13	0.11	0.13	0.12	0.21	0.17	0.25	0.21	0.32
Yb	0.05	2.63	2.26	1.15	1.14	1.55	2.02	1.77	1.07	1.38	1.31	1.31	1.49	1.37	0.72	1.84	1.37
Lu	0.01	0.39	0.33	0.11	0.18	0.34	0.23	0.29	0.19	0.2	0.19	0.21	0.25	0.22	0.25	0.29	0.11
ΣREE	-	180.45	160.14	195.01	150.65	193.53	158.44	120.86	154.65	150.81	151.89	151.87	138.39	145.20	154.29	156.22	148.85

values for other samples are less than 14.53. A similar trend is also observed for the Nb/Ta values of the argillic samples. The Nb/Ta values of N-7, N-8 and N-9 samples vary from 6.76 to 10.78, whereas the values of this ratio for the other samples vary from 11.09 to 18.71 (Table 3).

The REE contents of the samples from the argillic zone were normalized to the chondrite values proposed by Anders and Grevesse (1989). The chondrite-normalized distribution curves of the lithic crystal tuff and the argillic samples of the Jizvan district are illustrated in Fig. 8a and 8b, respectively. As Fig. 8a shows, the lithic crystal tuff samples are enriched in LREE so that the La/Lu values lie within the range of 10.57–10.82. The chondrite-normalized REE distribution curves of the argillic samples are shown in Fig. 8b. As this figure illustrates, the argillic samples are enriched in LREE, relative to MREE and HREE, with a marked tetrad effect phenomenon in the third and fourth tetrads. The La/Lu values of these samples vary within the range of 8.25–37.74 (Table 3). LREE enrichment during hydrothermal alteration can be related to open systems (Irber, 1999). Therefore, it can be inferred that structural controls such as fault breccia zones acted as hydrothermal channels during the alteration of the lithic crystal tuffs (as parent rocks) in the Jizvan district. Similar mechanisms for argillic alteration zones in El Seboah acidic peralkaline rocks (Egypt) were also reported by Abu Elatta Abdallah et al. (2014). As mentioned above, the non-CHARAC behavior of geochemical pairs can be related to tetrad effect, therefore, it can be concluded that tetrad effect is another important factor controlling the distribution of trace elements such as Nb, Ta, Zr, Hf and Y, as well as REE, in this district.

Among REE, Ce is an oxidation-sensitive element. This means that the Ce anomaly is strongly controlled by the fugacity of oxygen during geochemical processes. Increasing Paleogene oxygen fugacity in an environment causes Ce^{3+} to become oxidized to Ce^{4+} which has a smaller ionic radius and greater charge. Studies have

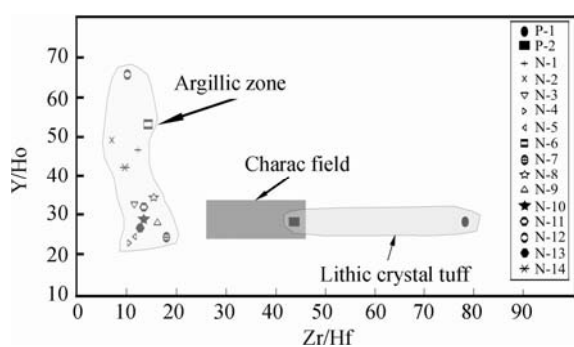


Fig. 7. Diagram of Zr/Hf versus Y/Ho for samples of the lithic crystal tuffs and the argillic zone in the Jizvan district. The Charac field is from Bau (1996).

Table 3 Computed geochemical parameters and the tetrad effect values of the studied samples from the lithic crystal tuffs (samples P-1, P-2) and the argillic alteration zone (samples N-1 to N-14) in the Jizvan district

Sample No	P-1	P-2	N-1	N-2	N-3	N-4	N-5	N-6	N-7	N-8	N-9	N-10	N-11	N-12	N-13	N-14
Ce anomaly	0.94	1.00	0.81	0.52	1.03	0.67	0.87	0.97	0.80	0.87	0.81	0.83	0.84	0.77	0.77	0.65
Eu anomaly	1.01	0.99	0.75	0.69	0.23	0.31	0.57	0.67	0.35	0.53	0.45	0.54	0.54	0.26	0.54	0.45
T ₃ tetrad effect	0.02	0.04	0.58	0.24	0.53	0.44	0.39	0.15	0.75	0.38	0.55	0.27	0.28	0.38	0.82	1.01
T ₄ tetrad effect	0.02	0.00	0.17	0.15	0.09	0.13	0.05	0.19	0.45	0.32	0.41	0.13	0.22	0.42	0.15	0.40
T ₁	0.14	0.15	0.61	0.44	0.56	0.53	0.47	0.41	0.78	0.59	0.70	0.45	0.50	0.63	0.70	0.84
LREE	162.06	144.83	180.98	135.15	171.90	144.47	100.25	137.95	131.72	133.99	133.33	119.16	126.63	138.06	132.23	133.31
HREE	18.39	15.31	14.03	15.50	21.63	13.97	20.61	16.70	19.09	17.90	18.54	19.23	18.57	16.23	23.99	15.54
LREE/HREE	8.81	9.46	12.90	8.72	7.95	10.34	4.86	8.26	6.90	7.49	7.19	6.20	6.82	8.51	5.51	8.58
La/Lu	10.57	10.82	37.74	12.19	9.84	12.38	8.25	12.81	12.17	12.75	11.88	10.52	11.53	9.98	9.46	25.23
Zr/Hf	78.67	43.03	12.16	6.72	11.48	10.28	11.66	14.53	17.82	15.37	16.02	13.43	13.18	10.07	12.62	9.49
Nb/Ta	11.36	11.09	16.43	14.22	18.71	14.67	18.00	14.56	7.67	10.78	10.44	11.09	13.50	16.43	15.14	15.63
Y/Ho	27.98	28.52	46.77	48.97	32.73	22.90	24.63	53.23	24.63	34.74	28.29	28.48	32.14	65.91	26.60	42.16

shown that Ce^{4+} in most geological environments is less mobile (Hannigan et al., 2010; Abedini and Calagari, 2013; Kraemer et al., 2016). The existence of a positive Ce anomaly in zircon is attributed to a higher oxygen fugacity during deposition (Burnham and Berry, 2014). The Ce anomaly values for the lithic crystal tuffs vary from 0.94 to 1.00. Based upon these values and the presence of zircon in the lithic tuff samples, it can be deduced that the lithic crystal tuffs have been formed under relatively high oxygen fugacity conditions. In contrast, the Ce anomalies of the argillic zone display relatively moderate negative anomalies (0.52–0.97), except in sample N-3 (1.03). This means that solutions with a low pH and high oxygen fugacity were most likely responsible for the alteration of the lithic crystal tuffs (Fulignati et al., 1999).

Eu, as an oxidation-sensitive element, has two oxidation states, Eu^{2+} and Eu^{3+} , during geochemical processes. Based on SHAB theory (Dai, 1987; Qicong and Congqiang, 2010), in low oxygen fugacity (almost reducing) environments, Eu^{2+} , along with soft bases such as HS^- , S^{2-} and CH_4 are commonly formed. Thus, Eu^{2+} can form more stable complexes and precipitate from solutions or fluids after being oxidized to Eu^{3+} (Tang et al., 2013). This is quite consistent with the analytical results of the lithic crystal tuff samples, which contain pyrite and show Eu anomalies within the range 0.99–1.01. Therefore, it can be deduced that the lithic crystal tuffs in the Jizvan district were likely formed under oxidizing conditions, and the slight positive Eu anomaly was due to the destruction of some minerals, such as plagioclase, potassium feldspar and hornblende, by hydrothermal fluids. In contrast, the Eu anomaly values in all of the argillic samples are relatively negative (0.23–0.75). Based on SHAB theory, a higher oxygen fugacity (oxidizing conditions) in the environment causes Eu^{3+} to be formed, and under these conditions hard bases such as OH^- , SO_4^{2-} and CO_3^{2-} are more prevalent. Consequently, rocks deposited under such conditions are characterized by a negative Eu anomaly. This can be reasonably generalized to the argillic zone in the Jizvan district. Abedini et al.

(2016) demonstrated that a relatively strong Eu anomaly can be related to low pH condition (a highly acidic environment) in hydrothermal systems. Therefore, it can be inferred that the argillic zone in the Jizvan district was probably formed by solutions having a relatively higher oxygen fugacity with a low pH.

5.2 Tetrad effect phenomenon

The chondrite-normalized REE distribution patterns in the lithic crystal tuff and the argillic samples in the Jizvan district display a tetrad effect in the form of M- and W-shaped patterns in the 3rd and 4th tetrads (Fig. 9). In order to investigate the size of the tetrad effect in distribution curves, mathematical equations have been proposed for quantification of the third and fourth tetrads (e.g., Irber, 1999; Monecke et al., 2002). By these mathematically-based methods, the values of the tetrad effect can be calculated for the first, the second, the third and the fourth tetrads, represented by T_i (where 'i' indicates the tetrad group). T_i indicates the deviation of the second and the third elements of each tetrad group from the straight line which connects the first and the fourth elements of the same tetrad group. When there is no tetrad effect ($T_i = 0$), all elements of a group lie on the straight line. $T_i > 0$ reflects the presence of a tetrad effect in the same group of elements. The values of T_i and T_t can be computed by applying the following equations (Monecke et al., 2002):

$$T_i = \frac{1}{\sqrt{2}} \times \left(\left[\frac{C_{Bi}}{\sqrt[3]{C_{Ai}^2 \times C_{Di}}} - 1 \right]^2 + \left[\frac{C_{Ci}}{\sqrt[3]{C_{Di}^2 \times C_{Ai}}} - 1 \right]^2 \right) \quad (3)$$

$$T_t = \sqrt{\left(\frac{1}{2N} \times \sum_{i=1}^N \left(\left[\frac{C_{Bi}}{\sqrt[3]{C_{Ai}^2 \times C_{Di}}} - 1 \right]^2 + \left[\frac{C_{Ci}}{\sqrt[3]{C_{Di}^2 \times C_{Ai}}} - 1 \right]^2 \right) \right)} \quad (4)$$

In the equations (3) and (4), C_{Ai} , C_{Bi} , C_{Ci} , and C_{Di} are the concentration values of the first, the second, the third and the fourth elements of each tetrad group, respectively. Meanwhile, the total value (T_t) can be calculated by using the T_i values (Equ. 4). T_t can be obtained by calculated values of the 2nd or the 3rd tetrads. T_i should not be calculated, if a Ce anomaly exists in the chondrite-

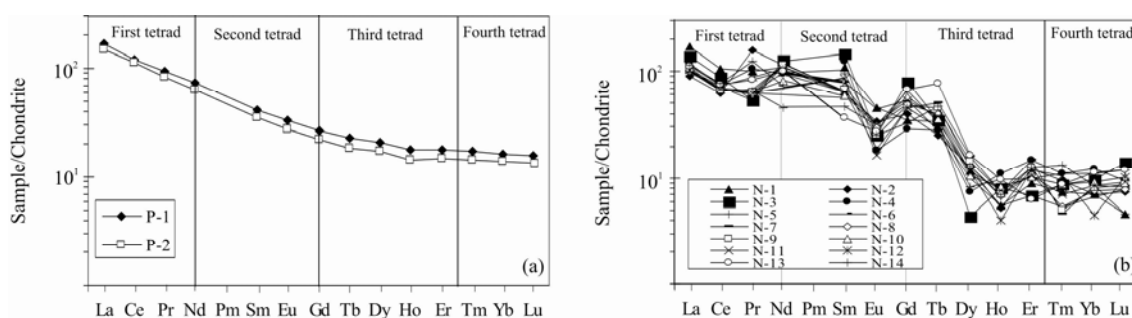


Fig. 8. Representation of the chondrite-normalized REE distribution patterns in samples from (a) the lithic crystal tuffs and (b) the argillic zone of the Jizvan district. Chondrite values are from Anders and Grevesse (1989).

normalized REE distribution patterns (Monecke et al., 2002). Pm does not occur in natural environments, therefore T_2 (the size of the second tetrad effect) should also not be calculated (McLennan, 1994).

Table 3 lists the calculated T_3 and T_4 values for the samples from the lithic crystal tuffs and the argillic zone in the Jizvan district. In this research, equations 3 and 4 were used to calculate the size of T_3 and T_4 . Meanwhile, the chondrite values applied for normalization are from Anders and Grevesse (1989). The graphic representation of the chondrite-normalized REE distribution curves and the computed T_3 and T_4 values of all samples are illustrated in Fig. 9. For clarity, the diagrams are provided separately (Fig. 9a–f). As represented in Fig. 9a, the lithic crystal tuff samples are characterized by very low T_3 and T_4 values which vary from 0.00 to 0.04, reflecting a slight M-shaped tetrad effect in the third and the fourth tetrads. As shown in Fig. 9b–f, all samples in the argillic zone are characterized by both convex (M-shaped) and concave (W-shaped) tetrad effect phenomena in the third and fourth tetrads of the chondrite-normalized REE patterns. The sizes of the third (T_3) and the fourth (T_4) tetrads are within the range of 0.15–1.01 (Fig. 10a) and 0.05–0.45 (Fig. 10b), respectively. The computed sizes of the third tetrad effect (T_3) along the studied profile vary across a wide range (Fig. 10a). In

contrast, the computed sizes of the fourth tetrad effect (T_4) have a narrow range. Thus, in this research, the computed sizes of the fourth tetrad effect (T_4) were used to investigate the geochemical processes and interpretations. The diagram of the frequency distribution of the sizes of the fourth tetrad effect (T_4) at Jizvan (Fig. 11a) displays a pronounced trimodal pattern, which can be attributed to various geochemical factors, such as different mineralization phases and the presence of solutions/fluids of a variety of compositions (Badel et al., 2011).

Understanding the geochemical processes using statistical data analysis reveals hidden patterns that are useful for geochemical models and processes involving evolution of systems (Wang et al., 2017). Cluster center updating and classification (*k*-means) are two methods for clustering the set of available data. In this research, clusters (characterized by similar properties) of the available data were classified on the basis of combining the geological relationships and field observations, such as lithologies and structural features, with computed clusters using the *k*-means method with the MATLAB R2016b computer software. The T_4 tetrad effect values show three separate populations. The first population (Fig. 11b), which belongs to the lithic crystal tuff samples, have very low T_4 values (median = 0.01). The second population, which pertains to

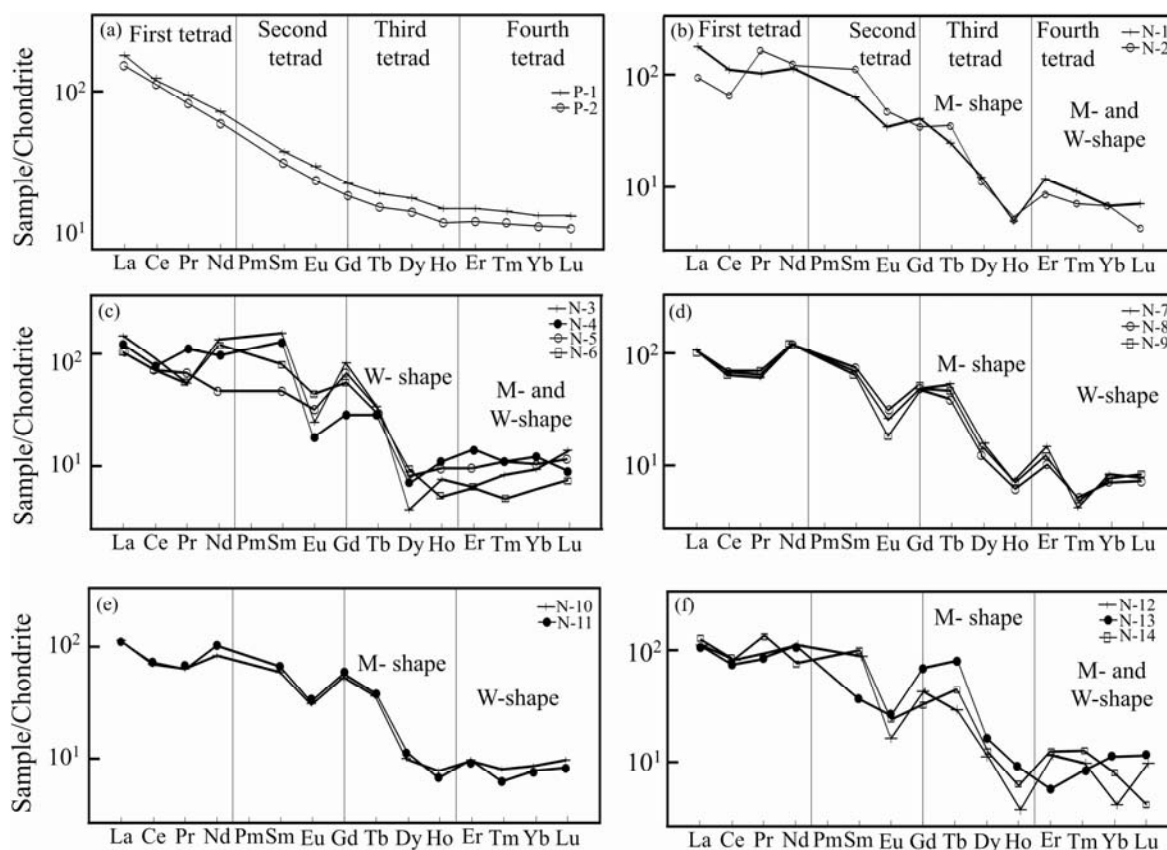


Fig. 9. Diagrams of the chondrite-normalized REE distribution patterns in collected samples.

(a), the lithic crystal tuffs (samples P-1, P-2); (b), for samples N-1 and N-2; (c), for samples from N-3 to N-6; (d), for samples N-7, N-8, and N-9; (e), for samples N-10 and N-11; and (f), for samples N-12, N-13, and N-14.

the argillic samples (Fig. 11c), displays relatively higher T_4 tetrad effect values (median of 0.14). Finally, the third population, represented by the argillic samples (Fig. 11d), displays greater T_4 values (median of 0.40).

The diagram of T_4 versus T_3 tetrad effect values (Fig. 12) illustrates three populations for the samples, which is quite consistent with the results of the clustering of the T_4 tetrad effect values (see Fig. 11). The diagram of T_4 versus T_3 , relating to the lithic crystal tuff samples, characteristically shows very low values for both tetrads (T_4 and T_3), which are similar to the first population of the T_4 tetrad effect frequency distribution. The second field in Fig. 12 belongs to the argillic samples with T_4 tetrad effect values less than 0.25 (median = 0.14). The third population, represented by the argillic samples, displays very high T_4 tetrad effect values.

5.3 Correlation of T_4 tetrad effect with geochemical indicators

The bivariate diagram of T_4 tetrad effect values versus Eu and Ce anomaly values for all samples of the studied profile (Fig. 13a–b), indicates that alteration of the lithic crystal tuffs likely occurred in different stages by various solutions/fluids with different compositions and/or temperature. As shown in Fig. 13a, the samples of the argillic alteration zone illustrate two distinct domains of data points. One domain, represented by the argillic samples, has relatively moderate to strong negative Eu anomalies and T_4 tetrad effect values of <0.22 . The second domain, which also belongs to the argillic samples, includes samples N-7, N-8, N-9, N12 and N-14, displaying moderate to strong negative Eu anomalies and T_4 tetrad effect values of >0.32 .

Decomposition of Eu-bearing minerals (feldspars) during hydrothermal activities can release Eu into solutions/fluids which is strongly mobile, and reduction of

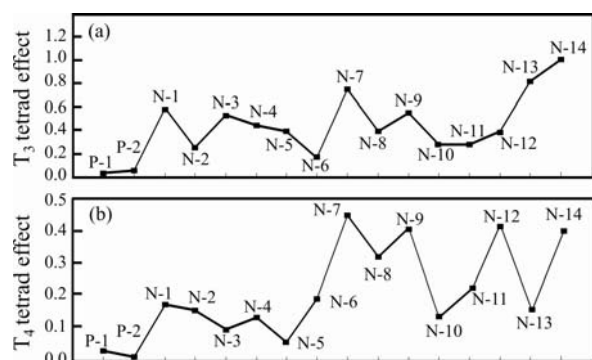


Fig. 10. Representation of the distribution patterns for T_3 and T_4 in samples from the lithic crystal tuffs (samples P-1, P-2) and the argillic alteration zone (samples from N-1 to N-14) of the Jizvan district.

(a), T_3 tetrad effect values in the studied profile; (b), T_4 tetrad effect values in the studied profile.

Eu^{3+} to Eu^{2+} can occur at temperatures $>200^\circ\text{C}$ (Schwinn and Markl, 2005). The moderate and negative Ce anomalies of the argillic samples (Fig. 13b) in the Jizvan district are due to the decomposition of zircon by fluids under acidic and oxidizing conditions (Fulignati, 1999). The presence of strongly negative Eu anomalies in some of the argillic samples (N-7, N-8 and N-9) from the fault zone with N12 and N-14 from the breccia zone leads us to conclude that hypogene hydrothermal fluids, having temperature $>200^\circ\text{C}$, low pH, and relatively high $f\text{O}_2$, were most likely responsible for the alteration of the lithic crystal tuffs. Meanwhile, the variation of U which is an oxidation-sensitive element, also shows that the U concentration in samples near to the fault zone (N-7, N-8, and N-9) of the studied area have lower values (an average of 2.83 ppm) and the U concentration increases towards the margin of the area (an average of 3.7 ppm). This implies that the fault system and breccia zone in the margin of the argillic deposit played significant roles as structural controllers in the development of the argillic zone.

Nb-Ta, Zr-Hf and Y-Ho are isovalent trace elements

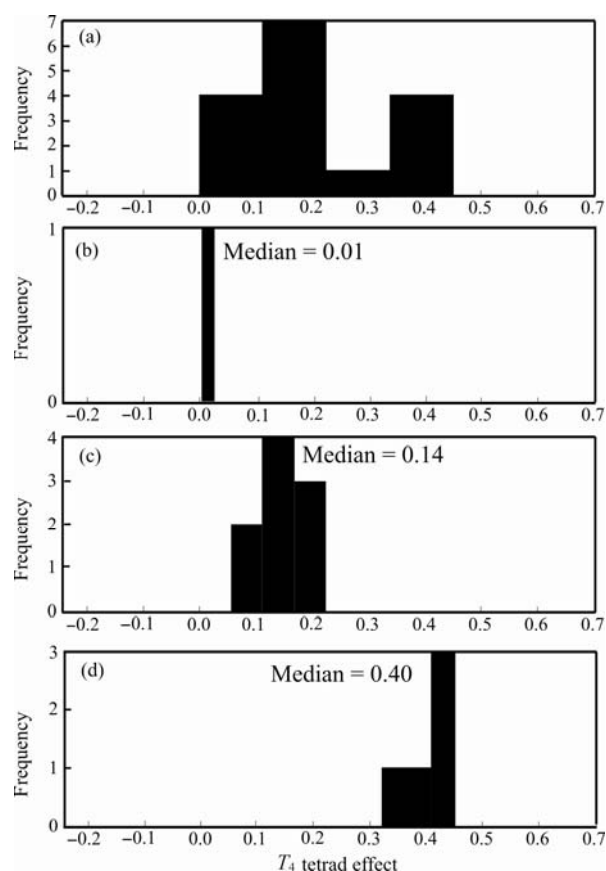


Fig. 11. Frequency distribution diagrams of the T_4 tetrad effect for all samples along the studied profile.

(a), The overall T_4 tetrad-effect; (b), The first population of the T_4 tetrad effect (median = 0.01); (c), The second population of the T_4 tetrad effect (median = 0.14); (d), The third population of the T_4 tetrad effect (median = 0.40).

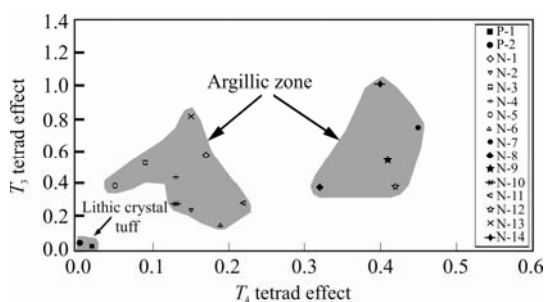


Fig. 12. Bivariate diagram of the T_4 versus T_3 tetrad effects in samples from the lithic crystal tuffs (samples P-1, P-2) and the argillic alteration zone (samples from N-1 to N14) in the Jizvan district, showing the domains of scattered data points.

with similar behaviors, which can be fractionated during geochemical processes such as hydrothermal activities (Bau, 1996; Irber, 1999; Ballouard et al., 2016). Previous studies have shown that isoivalent elements can be used to interpret the evolution of deposits (Gadd et al., 2016; Rezaei Azizi et al., 2017). In this research, the T_4 tetrad effect values versus geochemical ratios such as Zr/Hf (Fig. 14a), Nb/Ta (Fig. 14b) and Y/Ho (Fig. 14c) were plotted for the samples from the lithic crystal tuffs and the argillic alteration zone. As shown in Fig. 14, there are three groups of data points. The very low T_4 tetrad effect values (<0.02) belong to the lithic crystal tuff samples. The Zr/Hf ratios of the lithic crystal tuff samples are clearly higher than those of the argillic ones. This is certainly due to the presence of zircon within these samples. As shown in Fig. 14a, the argillic samples show two distinct sets of data points. One set has T_4 tetrad effect values <0.22 , and the other one has meaningfully higher T_4 tetrad-effect values (>0.30).

Variation of Nb/Ta values has been reported by many researchers from different geological environments (Tartese and Boulvais, 2010; Stepanov et al., 2014). Investigations conducted by Stepanov et al. (2014) showed that the solubility of Nb increases with the temperature of the hypogene fluids, and its abundance is related to the destruction of biotite (higher Nb content) in host rocks. As Fig. 14b displays, the Nb/Ta values of the studied argillic samples are high, reflecting the role of high temperature hypogene hydrothermal fluids, responsible for the alteration of the lithic crystal tuffs during development of the argillic zone. Minami et al. (1998) suggested that Y and Ho fractionation and the presence of remarkable conjugate convex and concave tetrad effects in the chondrite-normalized REE distribution patterns are characteristic of aqueous systems. As shown in Fig. 14c, the Y/Ho ratios of the argillic samples are also divided into two separate groups using T_4 tetrad effect values. The first group is characterized by low but variable

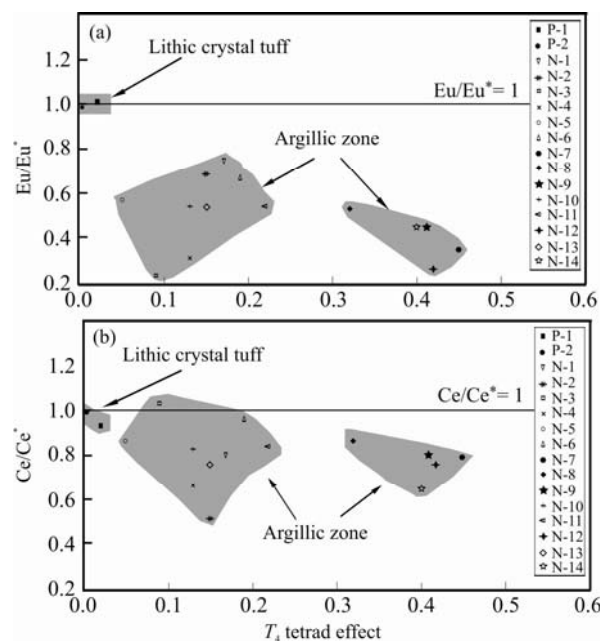


Fig. 13. Bivariate diagrams of the T_4 tetrad effect values. (a) Eu/Eu^* and (b) Ce/Ce^* in samples from the lithic crystal tuffs (samples P-1, P-2) and the argillic alteration zone (samples N-1 to N-14) in the Jizvan district. Shown in this figure are also the separate domains of the scattered data points.

T_4 tetrad effect values (<0.22). The second group has relatively higher T_4 tetrad effect values (<0.3), but with less variability. The main reason for the increasing values of the Y/Ho ratios in the argillic samples may be due to the preferential scavenging of Ho by Mn-oxides (Bau, 1996). Therefore, the relatively high values of Y/Ho in the argillic zone may be associated with the formation of Mn-oxides developed by supergene solutions.

Based on the above-mentioned discussions, it can be deduced that the argillic samples in the studied district are subdivided into two groups. One group represents samples from or near the fault zone. They show remarkably high T_4 tetrad effect values, and were produced by relatively high-temperature hypogene fluids. The other group includes samples farther from the fault zone. They have characteristically low T_4 tetrad-effect values, and probably were produced during rock-fluid interaction by low-temperature supergene and/or hydrothermal solutions. Thus, it further supports the fact that the computed T_4 tetrad effect values as geochemical parameters can be useful as a powerful indicator for the determination of the physico-chemical conditions of the fluids responsible for the alteration, and for the rock-fluid interaction mechanisms in geological environments.

5.4 The main mechanism for the tetrad effect

Various geochemical interpretations have been made for the presence of tetrad effects in different geological processes, including the formation of mineral phases,

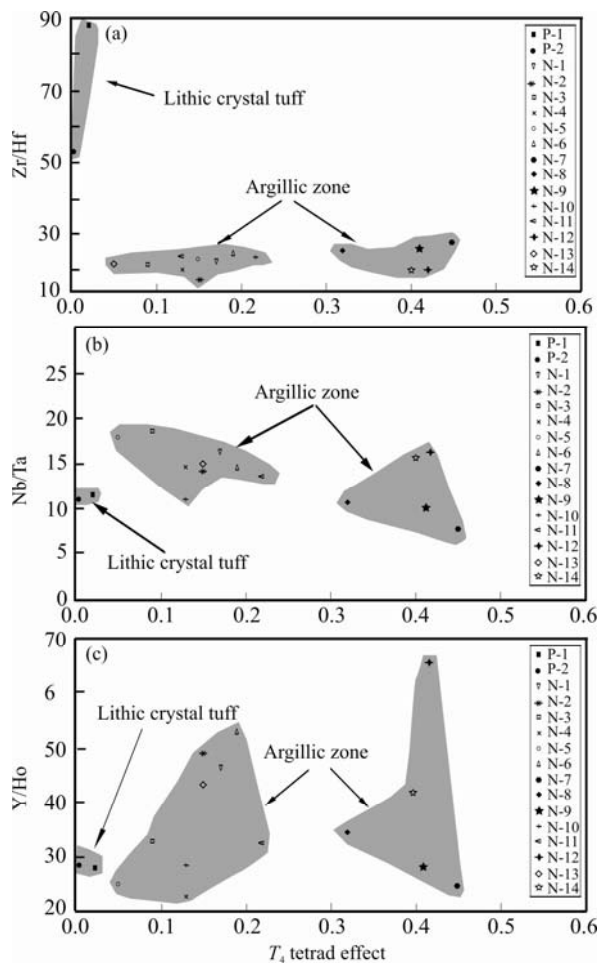


Fig. 14. Bivariate diagrams of the T_4 tetrad effect in samples from the lithic crystal tuffs (samples P-1, P-2) and the argillic alteration zone (samples N-1 to N-14) in the Jizvan district. Three discrete fields of data points are also shown in these diagrams.

(a), Zr/Hf ratios; (b), Nb/Ta ratios; and (c), Y/Ho ratios.

functions of complexes, fluid-rock interactions, weathering and hypogene alteration (Takahashi et al., 2002; Zhao et al., 2002; Monecke et al., 2007; Badanina et al., 2010). The M-shaped tetrad effect has been reported from most granites and igneous systems in which crystallization and fluid-rock interactions were suggested to be the main mechanisms for producing the tetrad effect (McLennan, 1994; Nardi et al., 2012).

According to the results illustrated in Fig. 15, there is a strong positive correlation ($r = 0.92$; with confidence level of 95%) between REE and MnO of the argillic samples. Hence, the existence of a typical M-shaped tetrad effect in the argillic samples can be related to mineral phases such as Mn-oxides and fluid-rock interaction during alteration of the lithic crystal tuffs.

Co-occurrence of convex (M-shaped) and concave (W-shaped) tetrad effects have been documented by many workers in various deposits such as the Toro uranium

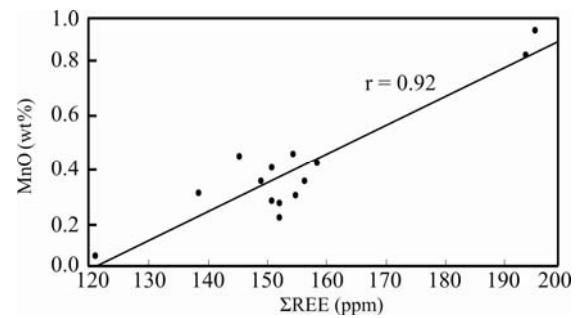


Fig. 15. Bivariate diagram showing the concentration values of SREE (ppm) against MnO (wt%) of the samples from argillic alteration in the Jizvan district.

deposit in Japan (Takahashi et al., 2002; Minuzzi et al., 2008), glasses in the Ary-Bula in Transbaikalia (Peretyazhko and Savina, 2010), the Qahr-Abad fluorite deposit in Iran (Rezaei Azizi et al. 2017), Terra rossa in China (Feng et al. 2011), and Ti-rich bauxites in Iran (Abedini et al., 2018). The surface weathering, alteration and/or fluid or solution mixing have been proposed as the main mechanisms for the tetrad effect in various environments (Kawabe et al., 1999; Feng et al., 2011). According to the results of the XRD analyses, the presence of goethite in the argillic zone (samples N-10 and N-13) can be related to weathering processes in this zone. On the other hand, the correlation of computed values for the T_4 tetrad effect versus geochemically isoivalent elemental pairs indicates that two fluids with contrasting temperature and/or composition were most likely to be responsible for the argillic alteration of the lithic crystal tuffs. This hypothesis is further supported by the coexistence of both the concave and convex tetrad effects in the argillic samples. This means that the mineral assemblages of the argillic alteration zone of the studied profile are the products of both hypogene hydrothermal activities and the overprinting supergene processes by which the lithic crystal tuffs were altered to predominantly clay minerals (Papoulis et al., 2004; Njoya et al., 2006; Fernández-Caliani et al., 2010). In other words, the high-temperature ascending hypogene fluid was likely the principal agent for alteration of the parent rocks (lithic crystal tuffs) along the fault and breccia zone. This is also supported by notably high T_4 tetrad effect values. Upon mixing of this hypogene fluid with low-temperature supergene solutions farther from the fault zone and in the breccia zone near the margin of the deposit, the argillic assemblages with low T_4 tetrad effect values were produced.

6 Conclusions

Based on the REE geochemistry, frequency distribution clusters, the values of tetrad effects, and correlation of

isovalent elemental pairs with T₄ tetrad effect values in the Jizvan district, the following conclusions can be drawn:

(1) Based on co-occurrence of both W- and M-type tetrad effects in the REE distribution patterns of the argillic samples, it can be concluded that scavenging by Mn-oxides, fluid-rock interaction, superimposition of the hypogene mineral assemblages by the supergene processes during alteration of the lithic crystal tuffs were the major mechanisms for the tetrad effects in the argillic alteration zone.

(2) Ce and Eu anomalies of the studied samples reveal that the decomposition of minerals such as feldspars and zircon under oxic conditions by hot and acidic fluids may be the main mechanism for generating the negative anomalies during alteration of the lithic crystal tuffs.

(3) The frequency distribution diagram of the T₄ tetrad effect in the studied district delineates three separate populations for samples representing the lithic crystal tuffs (the parent rocks), the argillic alteration zone in the fault zone, and the argillic halo farther from the fault zone near the breccia zone.

(4) As illustrated in the diagrams of T₄ tetrad effect values versus Y/Ho, Nb/Ta and Zr/Hf ratios, it can be deduced that mixing of the low-temperature supergene solutions with the high-temperature hypogene fluids during alteration of the lithic crystal tuffs are likely to be the main mechanism for the development of the argillic alteration zone.

(5) According to the obtained data, the computed T₄ tetrad effect values of the studied samples have proved to be a powerful indicator for the interpretation of the geochemical processes and also the determination of the physico-chemical conditions of the fluids involved during the argillic alteration of the lithic crystal tuffs.

Acknowledgments

This work was supported financially by the Research Bureau of Urmia University. The authors would like to express their thanks and gratitude to the authorities of this bureau. Our gratitude is further expressed to Prof. Degan Shu, Dr. Lian Liu, and two other anonymous reviewers for reviewing our manuscript and making critical comments and valuable suggestions which have definitely improved the quality of this work.

Manuscript received Dec. 6, 2017

accepted Jan. 12, 2018

edited by Fei Hongcai

References

Abedini, A., and Calagari, A.A., 2013. Rare earth elements

geochemistry of Sheikh-Marut laterite deposit, NW Mahabad, West-Azarbaidjan Province, Iran. *Acta Geologica Sinica* (English Edition), 87(1): 176–185.

Abedini, A., and Calagari, A.A., 2015. Geochemical characteristics of the Abgarm kaolin deposit, NW Iran. *Jahrbuch für Geologie und Paläontologie – Abhandlungen*, 278: 33–350.

Abedini, A., and Calagari, A.A., 2016. Geochemical characteristics of the Arabshah kaolin deposit, Takab geothermal field, NW Iran. *Arabian Journal of Geosciences*, 9 (548): 1–16.

Abedini, A., Calagari, A.A., and Naseri, H., 2016. Mineralization and REE geochemistry of hydrothermal quartz and calcite of Helmesi vein-type copper deposit, NW Iran. *Neues Jahrbuch für Geologie und Paläontologie – Abhandlungen*, 281: 123–134.

Abedini, A., Calagari, A.A., and Rezaei Azizi, M., 2018. The tetrad-effect in rare earth elements distribution patterns of titanium-rich bauxites: Evidence from the Kanigorgeh deposit, NW Iran. *Journal of Geochemical Exploration*, 186: 129–142.

Abedini, A., Rezaei Azizi, M., Calagari, A.A., and Cheshmehsari, M., 2017. Rare earth element geochemistry and tetrad effects of the Dalir phosphatic shales, northern Iran. *Neues Jahrbuch für Geologie und Paläontologie – Abhandlungen*, 286: 169–188.

Abu Elatta Abdallah, S., Ali Mohamed, G., and Bakry, A.R., 2014. Rare Metal Mineralization (Zr, U, Th, REE) Associated to El Seboah Acidic Peralkaline Rocks, South Western Desert of Egypt: Recovery Technique. *American Journal of Earth Sciences*, 1: 73–85.

Akagi, T., Hashimoto, Y., Fu F-F, Tsuno, H., Tao, H., and Nakano, Y., 2004. Variation of the distribution coefficients of rare earth elements in modern coral-lattices: Species and site dependencies. *Geochimica et Cosmochimica Acta*, 68: 2265–2273.

Anders, E., and Grevesse, N., 1989. Abundances of the elements: Meteoritic and solar. *Geochimica et Cosmochimica Acta*, 53: 187–214.

Azizi, H., and Moinevaziri, H., 2009. Review of the tectonic setting of Cretaceous to Quaternary volcanism in northwestern Iran. *Journal of Geodynamics*, 47: 167–179.

Badanina, E.V., Syritso, L.F., Volkova, E.V., Thomas, R., and Trumbull, R.B., 2010. Composition of Li-F granite melt and its evolution during the formation of the ore-bearing Orlovka massif in Eastern Transbaikalia. *Petrology*, 18: 131–157.

Badel, M., Angorani, S., and Shariat Panahi, M., 2011. The application of median indicator kriging and neural network in modeling mixed population in an iron ore deposit. *Computers and Geosciences*, 37: 530–540.

Ballouard, C., Poujol, M., Boulvais, P., Branquet, Y., Tartese, R., and Vigneresse, J.L., 2016. Nb-Ta fractionation in peraluminous granites: a marker of the magmatic-hydrothermal transition. *Geology*, 44: 231–234.

Bau, M., 1996. Controls on the fractionation of isovalent trace elements in magmatic and aqueous systems: evidence from Y/Ho, Zr/Hf, and lanthanide tetrad effect. *Contributions to Mineralogy and Petrology*, 123: 323–333.

Bau, M., and Dulski, P., 1995. Comparative study of yttrium and rare earth element behaviors in fluorine-rich hydrothermal fluids. *Contributions to Mineralogy and Petrology*, 119: 213–223.

- Bau, M., Koschinsky, A., Dulski, P., and Hein, J.R., 1996. Comparison of the partitioning behaviours of yttrium, rare earth elements, and titanium between hydrogenetic marine ferromanganese crusts and seawater. *Geochimica et Cosmochimica Acta*, 60: 1709–1725.
- Burnham, A.D., and Berry A.J., 2014. The effect of oxygen fugacity, melt composition, temperature and pressure on the oxidation state of cerium in silicate melts. *Chemical Geology*, 366: 52–60.
- Calagari, A.A., 2004. Geology and fracture-related hypogene hydrothermal alteration and mineralization of porphyry copper deposit at Sungun, Iran. *Journal of the Geological Society of India*, 64: 595–618.
- Censi, P., Sortino, F., Zuddas, P., Saiano, F., Brusca, L., Chiavetta, S., and Falcone, E.E., 2016. Rare earths behaviour during the deposition of volcanic sublimates. *Journal of Volcanology and Geothermal Research*, 33: 53–63.
- Censi, P., Sprovieri, M., Saiano, F., Di Geronimo, S.I., Larocca, D., and Placenti, F., 2007. The behaviour of REEs in Thailand's Mae Klong estuary: Suggestions from the Y/Ho ratios and lanthanide tetrad effects. *Estuarine, Coastal and Shelf Science*, 71: 569–579.
- Chandrasekhar, S., and Ramaswamy, S., 2007. Investigation on a gray kaolin from south east India. *Applied Clay Science*, 37: 32–46.
- Dai, A.B., 1987. *Coordination Chemistry*. Science Press, Beijing, 1–870 (in Chinese).
- Darabi-Golestan, F., and Hezarkhani, A., 2016. High precision analysis modeling by backward elimination with attitude on interaction effects on Au (Ag)-polymetallic mineralization of Glojeh, Iran. *Journal of African Earth Sciences*, 124: 505–516.
- Dill, H.G., Dohrmann, R., Kaufhold, S., and Çiçek, G., 2015. Mineralogical, chemical and micromorphological studies of the argillic alteration zone of the epithermal gold deposit Ovacik, Western Turkey: Tools for applied and genetic economic geology. *Journal Geochemical Exploration*, 148: 105–27.
- Dominguez, E.A., Iglesias, C., Dondi, M., and Murray, H.H., 2010. Genesis of the La Espingarda kaolin deposit in Patagonia. *Applied Clay Science*, 47: 290–302.
- Ekosse, G., 2001. Provenance of the Kgwakgwe kaolin deposit in Southeastern Botswana and its possible utilization. *Applied Clay Science*, 20: 137–152.
- Elliott, P.E., and Drohan, P.J., 2009. Clay accumulation and argillic-horizon development as influenced by aeolian deposition vs. local parent material on quartzite and limestone-derived alluvial fans. *Geoderma*, 151: 98–108.
- El-Mezayen, A.M., El-Feky, M.G., Omar, S.A., and Ibrahim, S.A.E.A., 2015. Geochemistry and a composite M-type with W-type of REE tetrad effect in altered granites of Abu Furad area, Central Eastern Desert, Egypt. *Greener Journal of Geology and Earth Sciences*, 3: 13–29.
- Feng, J.L., Zhao, Z.H., Chen, F., and Hu, H.P., 2014. Rare earth elements in sinters from the geothermal waters (hot springs) on the Tibetan Plateau, China. *Journal of Volcanology and Geothermal Research*, 287: 1–11.
- Feng, J.L., 2010. Behaviour of rare earth elements and yttrium in ferromanganese concretions, gibbsite spots, and the surrounding terra rossa over dolomite during chemical weathering. *Chemical Geology*, 271: 112–132.
- Feng, J.L., Gao, S.P., and Zhang, J.F., 2011. Lanthanide tetrad effect in ferromanganese concretions and terra rossa overlying dolomite during weathering. *Chemie der Erde-Geochemistry*, 71: 349–362.
- Fernández-Caliani, J.C., Galán, E., Aparicio, P., Miras, A., Márquez, and M.G., 2010. Origin and geochemical evolution of the Nuevo Montecastelo kaolin deposit (Galicia, NW Spain). *Applied Clay Science*, 49: 91–97.
- Fidelis, I., and Siekierski, S., 1966. The regularities in stability constants of some rare earth complexes. *Journal of Inorganic and Nuclear Chemistry*, 28: 185–188.
- Fulignati, P., Gioncada A. and Sbrana A., 1999. Rare earth element (REE) behaviour in the alteration facies of the active magmatic-hydrothermal system of Vulcano (Aeolian Islands, Italy). *Journal of Volcanology and Geothermal Research*, 88: 325–342.
- Gadd, M.G., Layton-Matthews, D., and Peter, J.M., 2016. Non-hydrothermal origin of apatite in SEDEX mineralization and host rocks of the Howard's Pass district, Yukon, Canada. *American Mineralogist*, 101: 1061–1071.
- Hannigan R., Dorval E., and Jones C., 2010. The rare earth element chemistry of estuarine surface sediments in the Chesapeake Bay. *Chemical Geology*, 272: 20–30.
- Irber, W., 1999. The lanthanide tetrad effect and its correlation with K/Rb, Eu/Eu*, Sr/Eu, Y/Ho, and Zr/Hf of evolving peraluminous granite suites. *Geochimica et Cosmochimica Acta*, 63: 489–508.
- Jafarzadeh, M., Harami, R.M., Friis, H., Amini, A., Mahboubi, A. and Lenaz, D., 2014. Provenance of the Oligocene–Miocene Zivah Formation, NW Iran, assessed using heavy mineral assemblage and detrital clinopyroxene and detrital apatite analyses. *Journal of African Earth Sciences*, 89: 56–71.
- Jahn, B.M., Wu, F., Capdevila, R., Martineau, F., Zhao, Z., and Wang, Y., 2001. Highly evolved juvenile granites with tetrad REE patterns: the Woduhe and Baerzhe granites from the Great Xing'an Mountains in NE China. *Lithos*, 59: 171–198.
- Jørgensen, C. K., 1970. The "tetrad effect" of Peppard is a variation of the nephelauxetic ratio in the third decimal. *Journal of Inorganic and Nuclear Chemistry*, 32: 3127–3128.
- Kawabe, I., Ohta, A., Ishii, S., tokumura, M., and Miyauchi, K., 1999. REE partitioning between Fe-Mn oxyhydroxide precipitates and weakly acid NaCl solutions: Convex tetrad effect and fractionation of Y and Sc from heavy lanthanides. *Geochemical Journal*, 33: 167–180.
- Kawabe, I., Ohta, A., Ishii, S., tokumura, M., and Miyauchi, K., 1999. REE partitioning between Fe-Mn oxyhydroxide precipitates and weakly acid NaCl solutions: convex tetrad effect and fractionation of Y and Sc from heavy lanthanides. *Geochemical Journal*, 33: 167–180.
- Khalatbari-Jafari, M., Juteau, T., Bellon, H., Whitechurch, H., Cotton, J., and Emami, M.H., 2003. New geological, geochronological and geochemical investigations of the Khoy ophiolites and related formations, NW Iran. *Journal of Asian Earth Sciences*, 23: 507–535.
- Koschinsky, A., Stascheit, A., Bau, M., and Halbach, P., 1997. Effects of phos-phatization on the geochemical and mineralogical composition of marine ferromanganese crusts. *Geochimica et Cosmochimica Acta*, 61: 4079–4094.
- Kraemer, D., Tepe, N., Pourret, O., and Bau, M., 2016. Negative cerium anomalies in manganese (hydr)oxide precipitates due

- to cerium oxidation in the presence of dissolved siderophores. *Geochimica et Cosmochimica Acta*, 196: 197–208.
- Lee, S.G., Asahara, Y., Tanaka, T., Kim, N.H., Kim, K.H., Yi, K., Masuda, A., and Song, Y.S., 2010. La–Ce and Sm–Nd isotopic systematics of early Proterozoic leucogranite with tetrad REE pattern. *Chemical Geology*, 276: 360–373.
- Lee, S.G., Masuda, A., and Kim S.H., 1994. An early Proterozoic leuco-granitic gneiss with the REE tetrad phenomenon. *Chemical Geology*, 114: 59–67.
- Lerouge, C., Kunov, A., Fléhoc, C., Georgieva, S., Hikov, A., Lescuyer, J.L., Petrunov, R., and Velinova, N., 2006. Constraints of stable isotopes on the origin of alunite from advanced argillic alteration systems in Bulgaria. *Journal of Geochemical Exploration*, 90: 166–182.
- Lin, B., Chen, Y., Tang, J., Wang, Q., Song, Y., Yang, C., Wang, W., He, W., and Zhang, L., 2017. $^{40}\text{Ar}/^{39}\text{Ar}$ and Rb–Sr ages of the Tiegelongnan porphyry Cu–(Au) deposit in the Bangong Co–Nujiang metallogenic belt of Tibet, China: Implication for generation of super-large deposit. *Acta Geologica Sinica (English Edition)*, 91(2): 602–616.
- Liu, C.Q., and Zhang, H., 2005. The lanthanide tetrad effect in apatite from the Altay No. 3 pegmatite, Xingjiang, China: an intrinsic feature of the pegmatite magma. *Chemical Geology*, 214: 61–77.
- Masuda, A., Kawakami, O., Dohmoto, Y., and Takenaka, T., 1987. Lanthanide tetrad effects in nature: Two mutually opposite types W and M. *Geochemical Journal*, 21: 119–124.
- Masuda, A., Matsuda, N., Minami, M., and Yamamoto, H., 1994. Approximate estimation of the degree of lanthanide tetrad effect from precise but partially void data measured by isotope dilution and an electron configuration model to explain the tetrad phenomenon. *Proceedings of the Japan Academy*, 70B: 169–174.
- McLennan, S.M., 1994. Rare earth element geochemistry and the “tetrad” effect. *Geochimica et Cosmochimica Acta*, 58: 2025–2033.
- Mehrabi, B., Ghasemi Siani, M., Goldfarb, R., Azizi H., Ganerod, M., and Elizabeth Marsh, E., 2016. Mineral assemblages, fluid evolution, and genesis of polymetallic epithermal veins, Glojeh district, NW Iran. *Ore Geology Reviews*, 78: 41–57.
- Mehrabi, B., Siani, M.G., and Azizi, H., 2014. The genesis of the epithermal gold mineralization at North Glojeh veins, NW Iran. *International Journal of Sciences: Basic and Applied Research*, 15: 479–497.
- Minami, M., Masuda, A., Takahashi, K., Adachi, M., and Shimizu, H., 1998. Y–Ho fractionation and lanthanide tetrad effect observed in cherts. *Geochemical Journal*, 32: 405–419.
- Minuzzi, O.R.R., Neto, A.C.B., Formoso, M.L.L., Andrade, S., Janasi, V.A., and Flores, J.A., 2008. Rare earth element and yttrium geochemistry applied to the genetic study of cryolite ore at the Pitinga Mine (Amazon, Brazil). *Anais da Academia Brasileira de Ciências*, 80: 719–733.
- Monecke, T., Dulski, P., and Kempe, U., 2007. Origin of convex tetrads in rare earth element patterns of hydrothermally altered siliceous igneous rocks from the Zinnwald Sn–W deposit, Germany. *Geochimica et Cosmochimica Acta*, 71: 335–353.
- Monecke, T., Kempe, U., Monecke, J., Sala, M., and Wolf, D., 2002. Tetrad effect in rare earth element distribution patterns: a method of quantification with application to rock and mineral samples from granite-related rare metal deposits. *Geochimica et Cosmochimica Acta*, 66: 1185–1196.
- Monecke, T., Monecke, J., Mönch, W., and Kempe, U., 2000. Mathematical analysis of rare earth element patterns of fluorites from the Ehrenfriedersdorf tin deposit, Germany: Evidence for a hydrothermal mixing process of lanthanides from two different sources. *Mineralogy and Petrology*, 70: 235–256.
- Nabatian, G., Ghaderi, M., Neubauer, F., Honarmand, M., Liu, X., Dong, Y., Jiang, S., Quadet, A., and Bernroider, M., 2014. Petrogenesis of Tarom high-potassic granitoids in the Alborz–Azarbaijan belt, Iran: geochemical, U–Pb zircon and Sr–Nd–Pb isotopic constraints. *Lithos*, 184–187: 324–345.
- Nabavi, M., 1976. *A preface for geology of Iran*. Geological Survey of Iran Publication (in Persian), 1–105.
- Nardi, L.V.S., Formoso, M.L.L., Jarvis, K., Oliveira, L., Bastos Neto, A.C., and Fontana, E., 2012. REE, Y, Nb, U, and Th contents and tetrad effect in zircon from a magmatic-hydrothermal F-rich system of Sn-rare metalecroylite mineralized granites from the Pitinga Mine, Amazonia, Brazil. *Journal of South American Earth Sciences*, 33: 34–42.
- Njoya, A., Nkoumbou, C., Grosbois, C., Njopwouo, D., Njoya, D., Courtin-Nomade, A., Yvon, J., and Martin, F., 2006. Genesis of Mayouom kaolin deposit (western Cameroon). *Applied Clay Science*, 32: 125–140.
- Nozaki, Y., Zhang, Y.S., and Amakawa, H., 1997. The fractionation between Y and Ho in the marine environment. *Earth and Planetary Science Letters*, 148: 329–340.
- Papoulis, D., Tsolis-Katagas, P., and Katagas, C., 2004. Monazite alteration mechanisms and depletion measurements in kaolins. *Applied Clay Science*, 24: 271–285.
- Peppard, D.F., Mason, G.W., and Lewey, S., 1969. A tetrad effect in the liquid–liquid extraction ordering of lanthanide (III). *Journal of Inorganic and Nuclear Chemistry*, 31: 2271–2272.
- Peretyazhko, I.S., and Savina, E.A., 2010. Tetrad effects in the rare earth element patterns of granitoid rocks as an indicator of fluoride silicate liquid immiscibility in magmatic systems. *Petrology*, 18: 514–543.
- Pérez-López, R., Delgado, J., Nieto, J.M., and Márquez-García, B., 2010. Rare earth element geochemistry of sulphide weathering in the São Domingos mine area (Iberian Pyrite Belt): A proxy for fluid–rock interaction and ancient mining pollution. *Chemical Geology*, 276: 29–40.
- Lin, B., Chen, Y., Tang, J., Wang, Q., Song, Y., Yang, C., Wang, W., He, W. and Zhang, L., 2017. $^{40}\text{Ar}/^{39}\text{Ar}$ and Rb–Sr ages of the Tiegelongnan porphyry Cu–(Au) deposit in the Bangong Co–Nujiang metallogenic belt of Tibet, China: Implication for generation of super-large deposit. *Acta Geologica Sinica (English Edition)*, 91(2): 602–616.
- Ling Qicong and Liu Congqiang, 2010. Geochemical behaviors of REE and other trace elements during the formation of stratabound skarns and related deposits: A case study of the Dongguashan Cu (Au) deposit, Anhui Province, China. *Acta Geologica Sinica (English Edition)*, 77(2): 246–257.
- Rezaei Azizi, M., Abedini, A., Alipour, S., Niroomand, S., Sasmaz, A., and Talaei, B., 2017. Rare earth element geochemistry and tetrad effects in fluorites: A case study from the Qahr-Abad deposit, Iran. *Neues Jahrbuch für Geologie und Paläontologie – Abhandlungen*, 383: 255–273.
- Schwinn, G., and Markl, G., 2005. REE systematics in hydrothermal fluorite. *Chemical Geology*, 216: 235–248.

- Shannon, R.D., 1976. Revised effective ionic radii and systematic studies of interatomic distances in halides and chalcogenides. *Acta Crystallographica B*, 25: 925–946.
- Stepanov, A., Mavrogenes, J.A., Meffre, S., and David, S.P., 2014. The key role of mica during igneous concentration of tantalum. *Contributions to Mineralogy and Petrology*, 167: 1009–1016.
- Takahashi, Y., Yoshida, H., Sato, N., Hama, K., Yusa, Y., and Shimizu, H., 2002. W- and M-type tetrad effects in REE patterns for water–rock systems in the Tono uranium deposit, central Japan. *Chemical Geology*, 184: 311–335.
- Takahashia, Y., Chatellier, X., Hattorid, K.H., Kato, K., and Fortin, D., 2005. Adsorption of rare earth elements onto bacterial cell walls and its implication for REE sorption onto natural microbial mats. *Chemical Geology*, 219: 53–67.
- Tang, H.S., Chen, Y.J., Santosh, M., Zhong, H., and Yang, T., 2013. REE geochemistry of carbonates from the Guanmenshan Formation, Liaohe Group, NE Sino-Korean Craton: Implications for seawater compositional change during the Great Oxidation Event. *Precambrian Research*, 227: 316–336.
- Tang, M., Wang, X.L., Shu, X.J., Wang, D., Yang, T., and Gopon, P., 2014. Hafnium isotopic heterogeneity in zircons from granitic rocks: Geochemical evaluation and modeling of “zircon effect” in crustal anatexis. *Earth and Planetary Science Letters*, 389: 188–199.
- Tartese, R., and Boulvais, P., 2010. Differentiation of peraluminous leucogranites “en route” to the surface. *Lithos*, 114: 353–368.
- Uysal, I.T., Gasparon, M., Bolhar, R., Zhao, J.X., Feng, Y.X., and Jones, G., 2011. Trace element composition of near-surface silica deposits-A powerful tool for detecting hydrothermal mineral and energy resources. *Chemical Geology*, 280: 154–169.
- Veliz, H., Campos, E., Menzies, A., Valdivia, L., 2017. Relationship between hydrothermal alteration index and geological attributes at Chuquicamata Cu–Mo Porphyry Deposit, Chile. *Resource Geology*, 67: 158–173.
- Wang, J., Zuo, R., and Caers, J., 2017. Discovering geochemical patterns by factor-based cluster analysis. *Journal of Geochemical Exploration*, 181: 106–115.
- Watanabe, Y., Sato, R., Sulaksono, A., 2018. Role of Potassic Alteration for Porphyry Cu Mineralization: Implication for the Absence of Porphyry Cu Deposits in Japan. *Resource Geology*, 68: 195–207.
- Zhang, G.L., and Smith-Duque, C., 2014. Seafloor basalt alteration and chemical change in the ultra thinly sedimented South Pacific. *Geochemistry, Geophysics, Geosystem*, 15: 3066–3080.
- Zhao, Z.H., Xiong, X.L., Han, X.D., Wang, Y.X., Wang, Q., Bao, Z.W., and Jahn, B.M., 2002. Controls on the REE tetrad effect in granites: evidence from the Qianlishan and Baerzhe Granites, China. *Geochemical Journal*, 36: 527–543.

About the first author

Ali ABEDINI: an associate professor in the Department of Geology, Urmia University, Iran. He specialized in economic geology and geochemical exploration. He is the author and co-author of 220 papers on the geology of Iran.